Orientation, distribution, and deposition of elongated, inertial fibers in turbulent channel flow

Cristian Marchioli, Marco Fantoni, and Alfredo Soldati[a)]
Dipartimento di Energetica e Macchine and Centro Interdipartimentale di Fluidodinamica e Idraulica, Università degli Studi di Udine, 33100 Udine, Italy

(Received 1 August 2009; accepted 29 January 2010; published online 4 March 2010)

In this paper, the dispersion of rigid, highly elongated fibers in a turbulent channel flow is investigated. Fibers are treated as prolate ellipsoidal particles which move according to their inertia and to hydrodynamic drag and rotate according to hydrodynamic torques. The orientational behavior of fibers is examined together with their preferential distribution, near-wall accumulation, and wall deposition: all these phenomena are interpreted in connection with turbulence dynamics near the wall. In this work a wide range of fiber classes, characterized by different elongation (quantified by the fiber aspect ratio, λ) and different inertia (quantified by a suitably defined fiber response time, τ_p) is considered. A parametric study in the (λ, τ_p)-space confirms that, in the vicinity of the wall, fibers tend to align with the mean streamwise flow direction. However, this aligned configuration is unstable, particularly for higher inertia of the fiber, and can be maintained for rather short times before fibers are set into rotation in the vertical plane. A more complex situation is observed in the spanwise and wall-normal flow directions, where fiber inertia and elongation destabilize near-wall alignment in a nontrivial fashion. Fiber orientational behavior and fiber translational behavior are observed to influence the process of fiber accumulation at the wall. Comparing the behavior of fibers with that of spherical particles, it is observed that the aspect ratio has little or no effect on clustering, preferential distribution, and segregation; yet it does affect the wallward drift velocity of the fibers in such a way that longer fibers tend to deposit at higher rates. No preferential orientation and no significant segregation is observed in the channel centerline, confirming that the role of inertia and, in particular, of elongation becomes less important in and beyond the logarithmic layer.
 [doi:10.1063/1.3328874]

I. INTRODUCTION

Suspensions of tiny rigid fibers in turbulent flows are commonly encountered in a variety of industrial processes. Examples include pulp production and paper making, where controlling the rheological behavior and the orientation distribution of fibers is crucial to optimize production operations. In these processes, in particular, anisotropic fiber orientation induced by the carrier flow strongly influences the mechanical properties of manufactured paper. Elongated fibers also represent an interesting (and more feasible) alternative to the use of flexible polymers for reducing pressure drops in fluid transport systems, even though fibers yield lower drag reductions, they are more resistant to shear degradation and can be easily separated from the conveyed fluid at the end of the pipeline. Due to this practical importance, fiber dispersion in internal flows has been extensively investigated through experiments[1,2] and modeled using Fokker–Planck type equations.[1,3–6] Yet, a limited number of phenomenological studies based on accurate numerical simulations is available. As a result, different from the case of spherical particles, current knowledge of the mechanisms that are responsible for fibers-turbulence interaction is not satisfactory, and a deeper understanding of the physical problem is required.[6]

Restricting the discussion to Eulerian–Lagrangian studies, the first direct numerical simulation (DNS) relevant to the problem of turbulent fiber dispersion was performed by Zhang *et al.*;[7] followed by the complementary DNS of Mortensen *et al.*[8,9] Both works were focused on transport and deposition of prolate ellipsoidal particles in turbulent channel flow, and have shown that such elongated particles, similar to spherical particles, accumulate in the viscous sublayer and preferentially concentrate in regions of low-speed fluid velocity.[7–9] Being nonisotropic, ellipsoidal particles also tend to align with the mean flow direction, particularly very near the wall where their lateral tilting is suppressed.[7–9] In this paper, we build on these results and, starting from the same physical problem, we discuss new statistics to analyze the influence of near-wall turbulence on preferential distribution, wall deposition, and orientation state of rigid fibers, characterized by different elongation and different inertia. Our objective is to highlight the circumstances in which fibers behavior significantly deviates from that of spherical particles, in an effort to infer valuable conclusions significant to real situations including dilute air flows with velocity of a few meters per second in ducts with hydraulic diameters of a few centimeters, dilute water flows in microchannels, or fibrous aerosols transport in microgravity conditions.

Following Zhang *et al.*[7] and Mortensen *et al.*,[8,9] several

[a)]Author to whom correspondence should be addressed. Also at Department of Fluid Mechanics, CISM, 33100 Udine, Italy. Electronic mail: soldati@uniud.it.

assumptions are made in the simulations. For instance, fibers are approximated as noninteracting non-Brownian prolate ellipsoids immersed in a dilute flow without gravity. Also, lubrication or aggregation effects are ignored and fiber size is assumed less than the Kolmogorov length-scale. Despite these simplifications, however, the resulting lumped-parameter model provides a strong mathematical coupling between the translational motion and the rotational motion of fibers, as highlighted in Sec. II. Through this coupling, the hydrodynamic viscous drag force generated locally on the surface of a fiber depends explicitly on fiber orientation. This dependency is crucial to discriminate between elongated fibers and *equivalent* spherical particles of the same inertia (namely, of the same mass). Consider wall deposition for instance: drag resistance generated by a fiber which deposits moving parallel to the wall will be higher than that generated by its spherical equivalent or by a fiber of the same inertia which deposits moving perpendicular to the wall, with obvious effect on deposition rates. The same applies to fibers that either tumble or oscillate in their drift to the wall. This paper is intended to complete the current literature[7–9] on Lagrangian tracking of fibers adding new data in the parameter space (λ, τ_p and Re) and presenting new statistics to fully characterize fiber behavior.

II. METHODOLOGY

The Eulerian fluid dynamics is governed by the continuity and Navier–Stokes equations written for incompressible, isothermal, and Newtonian fluid. Equations in dimensionless form read as

$$\frac{\partial u_i}{\partial x_i} = 0, \tag{1}$$

$$\frac{\partial u_i}{\partial t} = -u_j \frac{\partial u_i}{\partial x_j} + \frac{1}{\mathrm{Re}_\tau}\frac{\partial^2 u_i}{\partial x_j^2} - \frac{\partial p}{\partial x_i} + \delta_{1,i}, \tag{2}$$

where u_i is the ith component of the velocity vector, p is the fluctuating kinematic pressure, $\delta_{1,i}$ is the mean pressure gradient that drives the flow and $\mathrm{Re}_\tau \equiv u_\tau h/\nu$ is the Reynolds number based on the shear (or friction) velocity, u_τ, and on the half channel height, h. The shear velocity is $u_\tau \equiv \sqrt{\tau_w/\rho}$, where τ_w is the mean shear stress at the wall. The superscript +, which is used in this paper to represent dimensionless variables, is dropped from Eqs. (1) and (2) for ease of reading. A pseudospectral flow solver is employed to solve such equations at a shear Reynolds number $\mathrm{Re}_\tau = 150$. The corresponding bulk Reynolds number is $\mathrm{Re} = u_b h/\nu = 2250$, where $u_b = 1.77$ m/s is the bulk velocity. The Reynolds number based on the hydraulic diameter is $\mathrm{Re}_D \simeq 9000$. The flow solver is based on the Fourier–Galerkin method in the streamwise (x) and spanwise (y) directions, whereas a Chebyshev-collocation method in the wall-normal direction (z). Time integration of fluid uses a second-order Adams–Bashforth scheme for the nonlinear terms (which are calculated in a pseudospectral way with dealiasing in the periodic directions) and an implicit Crank–Nicolson scheme for the viscous terms.[10,11] The size of the computational domain is $4\pi h \times 2\pi h \times 2h$ in x, y, and z, respectively; computations are carried out using $128 \times 128 \times 129$ grid points. Periodic boundary conditions are applied in x and y, no-slip conditions are enforced at both walls. The grid resolution is uniform in the homogeneous directions x and y, whereas a grid refinement (providing a minimum nondimensional grid spacing of 0.045 wall units) is applied near the walls in the nonhomogeneous direction, z. The nondimensional step size for time integration is 0.03 in wall units. Regarding the Lagrangian fiber dynamics, the dispersed phase is treated in the same way as in Refs. 7–9 and 12. The translational equation of motion of an individual fiber is given by the linear momentum equation $d\mathbf{u}_p/dt = \mathbf{F}/m$, where $\mathbf{u}_p$ is the fiber velocity, $\mathbf{F}$ is the total hydrodynamic drag force acting on the fiber, and $m = (4/3)\pi a^3 \lambda \rho_p$ is the fiber mass. Here a is the semiminor axis, $\lambda = b/a$ is the aspect ratio of the ellipsoid, b being the semimajor axis, and ρ_p is the density of the particle. The expression for $\mathbf{F}$ used in our simulations was first derived by Brenner[13] for an ellipsoid under creeping flow conditions: $\mathbf{F} = \mu \mathbf{K}(\mathbf{u}_{@p} - \mathbf{u}_p)$, where μ is the fluid dynamic viscosity, $\mathbf{K}$ is the resistance tensor (whose components depend on the orientation of the fiber through the four well-known Euler parameters) and $\mathbf{u}_{@p}$ is the fluid velocity at fiber position (obtained using a one-sided interpolation scheme based on sixth-order Lagrangian polynomials). The resistance tensor $\mathbf{K}$ is expressed with respect to the Eulerian (inertial) frame of reference, $\mathbf{x} = \langle x, y, z \rangle$. Two other Cartesian coordinate systems are used to describe fiber motion: a Lagrangian fiber frame of reference, $\mathbf{x}' = \langle x', y', z' \rangle$, attached to the fiber with origin at the fiber center of mass; and a comoving frame of reference, $\mathbf{x}'' = \langle x'', y'', z'' \rangle$, attached to the fiber with origin at the fiber center of mass and axes parallel to the inertial frame. Given these frames, the resistance tensor is computed as $\mathbf{K} = \mathbf{A}^t \mathbf{K}' \mathbf{A}$, where $\mathbf{K}'$ is the resistance tensor computed in the fiber frame, $\mathbf{A}$ is the orthogonal transformation matrix comprising the direction cosines (which, in turn, are defined by the Euler parameters), and $\mathbf{A}^t$ is its transpose. Matching the x', y', z' axes with the principal axes of resistance, tensor $\mathbf{K}'$ can be computed in diagonal form as[13]

$$\mathbf{K}' = \begin{bmatrix} k_{x'x'} & 0 & 0 \\ 0 & k_{y'y'} & 0 \\ 0 & 0 & k_{z'z'} \end{bmatrix}, \tag{3}$$

where the diagonal elements read as[12]

$$k_{x'x'} = k_{y'y'} = \frac{16(\lambda^2-1)^{3/2}}{[(2\lambda^2-3)\cdot \ln(\lambda + \sqrt{\lambda^2-1})] + \lambda\sqrt{\lambda^2-1}}, \tag{4}$$

$$k_{z'z'} = \frac{8(\lambda^2-1)^{3/2}}{[(2\lambda^2-1)\cdot \ln(\lambda + \sqrt{\lambda^2-1})] + \lambda\sqrt{\lambda^2-1}}. \tag{5}$$

The complete set of equations considered to describe translational and rotational motion of the fibers, written in dimensionless form, reads as:

$$\text{Kinematics}\begin{cases}\dfrac{\mathrm{d}\mathbf{x}_{p,(G)}}{\mathrm{d}t}=\mathbf{u}_p\\[2mm] \dfrac{\mathrm{d}e_0}{\mathrm{d}t}=\dfrac{1}{2}(-e_1\omega_{x'}-e_2\omega_{y'}-e_3\omega_{z'})\\[2mm] \dfrac{\mathrm{d}e_1}{\mathrm{d}t}=\dfrac{1}{2}(e_0\omega_{x'}-e_3\omega_{y'}+e_2\omega_{z'})\\[2mm] \dfrac{\mathrm{d}e_2}{\mathrm{d}t}=\dfrac{1}{2}(e_3\omega_{x'}+e_0\omega_{y'}-e_1\omega_{z'})\\[2mm] \dfrac{\mathrm{d}e_3}{\mathrm{d}t}=\dfrac{1}{2}(-e_2\omega_{x'}+e_1\omega_{y'}+e_0\omega_{z'})\end{cases}, \tag{6}$$

$$\text{Dynamics}\begin{cases}\dfrac{\mathrm{d}\mathbf{u}_p}{\mathrm{d}t}=\dfrac{3}{4\lambda Sa^2}\mathbf{K}\cdot(\mathbf{u}_{@p}-\mathbf{u}_p)\\[2mm] \dfrac{\mathrm{d}\omega_{x'}}{\mathrm{d}t}=\omega_{y'}\omega_{z'}\left(1-\dfrac{2}{1+\lambda^2}\right)+\dfrac{20[(1-\lambda^2)f'+(1+\lambda^2)(\xi'-\omega_{x'})]}{(\alpha_0+\lambda^2\gamma_0)(1+\lambda^2)Sa^2}\\[2mm] \dfrac{\mathrm{d}\omega_{y'}}{\mathrm{d}t}=\omega_{x'}\omega_{z'}\left(\dfrac{2}{1+\lambda^2}-1\right)+\dfrac{20[(\lambda^2-1)g'+(\lambda^2+1)(\eta'-\omega_{y'})]}{(\alpha_0+\lambda^2\gamma_0)(1+\lambda^2)Sa^2}\\[2mm] \dfrac{\mathrm{d}\omega_{z'}}{\mathrm{d}t}=\dfrac{20}{(2\alpha_0)Sa^2}(\chi'-\omega_{z'})\end{cases}, \tag{7}$$

where $\mathbf{x}_{p,(G)}$ is the fiber location vector (centered at the fiber center of mass G), e_i are the Euler parameters, ω_i are the fiber angular velocity components, and S is the fiber-to-fluid density ratio. Quantities f' and g' are elements of the fluid rate of strain tensor $S_{ij}=1/2(\partial u_i/\partial x_j+\partial u_j/\partial x_i)=1/2(u_{i,j}+u_{j,i})$ while ξ', η', and χ' are elements of the fluid rate of rotation tensor $\Omega_{ij}=1/2(u_{i,j}-u_{j,i})$, all expressed in the fiber frame

$$f'=\tfrac{1}{2}(u_{z',y'}+u_{y',z'}),\quad g'=\tfrac{1}{2}(u_{x',z'}+u_{z',x'}), \tag{8}$$

$$\xi'=\tfrac{1}{2}(u_{z',y'}-u_{y',z'}),\quad \eta'=\tfrac{1}{2}(u_{x',z'}-u_{z',x'}),$$
$$\chi'=\tfrac{1}{2}(u_{x',y'}-u_{y',x'}). \tag{9}$$

The parameters α_0, β_0, and γ_0 come from the equations derived by Jeffery[14] to compute the torque components for an ellipsoid subject to linear shear under creeping flow conditions (equations not shown) and are given as

$$\alpha_0=\beta_0=\frac{2\lambda^2\sqrt{\lambda^2-1}+\lambda\cdot\ln\left(\dfrac{\lambda-\sqrt{\lambda^2-1}}{\lambda+\sqrt{\lambda^2-1}}\right)}{2(\lambda^2-1)^{3/2}},$$
$$\gamma_0=\frac{2\sqrt{\lambda^2-1}+\lambda\cdot\ln\left(\dfrac{\lambda-\sqrt{\lambda^2-1}}{\lambda+\sqrt{\lambda^2-1}}\right)}{(\lambda^2-1)^{3/2}}. \tag{10}$$

Equations (6) are integrated in time using a standard fourth-order Runge–Kutta scheme, while Eq. (7) are solved using a mixed explicit/implicit differencing procedure developed by Fan and Ahmadi:[15] this procedure is specifically tailored for solving stiff ODEs. The same timestep size as that of the fluid is used for integration, and the total tracking time in wall units is $t^+=t\nu/u_\tau^2=1200$. Note that, for each particle at each timestep, the Euler parameters are renormalized according to

$$e_i=\frac{e_i}{\sqrt{e_0^2+e_1^2+e_2^2+e_3^2}} \tag{11}$$

to preserve the constraint $e_0^2+e_1^2+e_2^2+e_3^2=1$.

The relevant parameters to be specified for time integration are a, λ, and the fiber response time

$$\tau_p=\frac{2a^2S}{9\nu}\frac{\lambda\ln(\lambda+\sqrt{\lambda^2-1})}{\sqrt{\lambda^2-1}}. \tag{12}$$

The above definition for τ_p was derived by Shapiro and Goldenberg[16] based on the assumption of isotropic particle orientation and the inverse of the resistance tensor. In this study, we have selected the following dimensionless values: $a^+=0.36$, $\lambda=1.001$ (spherical particles), 3, 10, 50, and $\tau_p^+=1$, 5, 30, and 100, thus extending and completing the database of Mortensen *et al.*[8,9] to 16 cases in the (λ,τ_p^+)-space; see Table I. To ensure converged statistics, swarms of $N=200\,000$ fibers are tracked for each particle category, assuming dilute flow conditions (fiber volume fraction is always well below unity) and one-way coupling between the phases.

TABLE I. Summary of simulations and relevant particle parameters. The ellipsoid semimajor axis is given by b (b^+ in dimensionless form).

Set	τ_p^+	λ	S	$2b^+$	$2b$ (μm)	ρ_P (kg/m^3)
F1-1	1	1.001	34.72	0.72	96.07	45.14
F1-3	1	3	18.57	2.16	287.93	24.14
F1-10	1	10	11.54	7.20	960.09	15.01
F1-50	1	50	7.54	36.00	4800.01	9.80
F5-1	5	1.001	173.60	0.72	96.07	225.68
F5-3	5	3	92.90	2.16	287.93	120.77
F5-10	5	10	57.70	7.20	960.09	75.01
F5-50	5	50	37.69	36.00	4800.01	49.00
F30-1	30	1.001	1041.70	0.72	96.07	1354.21
F30-3	30	3	557.10	2.16	287.93	724.23
F30-10	30	10	346.30	7.20	960.09	450.19
F30-50	30	50	226.15	36.00	4800.01	294.00
F100-1	100	1.001	3472.33	0.72	96.07	4514.03
F100-3	100	3	1857.00	2.16	287.93	2414.10
F100-10	100	10	1154.33	7.20	960.09	1500.63
F100-50	100	50	753.83	36.00	4800.01	979.98

III. RESULTS AND DISCUSSION

A. Macroscopic fiber distribution and segregation

Figure 1 shows the instantaneous distribution of the $\tau_p^+=5$ fibers with $\lambda=50$, which are taken as reference for visualizations: similar distributions are observed for the other categories, but they are not shown in this paper for the sake of brevity. From Fig. 1(a) it is apparent that fibers cluster into groups leaving regions empty of fibers. As already noted by Mortensen *et al.*,[8] these regions have the same location for all the fiber categories investigated, and mark the position of the turbulent coherent vortices which govern the dispersion process. This indicates that, regardless of the strong mathematical coupling between rotational and translational equations due to the dependency of the resistance tensor on the orientation, macroscopic fiber distributions are practically unaffected by elongation and depend only on inertia (which, in our study, is always sufficient to centrifuge fibers out of the vortices core). From Fig. 1(b), it can also be observed that fibers tend to align according to the mean shear of the flow: in the channel centerline, where velocity gradients are low, fiber are more randomly oriented; near the wall, where velocity gradients are strong, fibers become more aligned with the wall. In this latter region, higher fiber number density is visible, indicating ongoing accumulation.

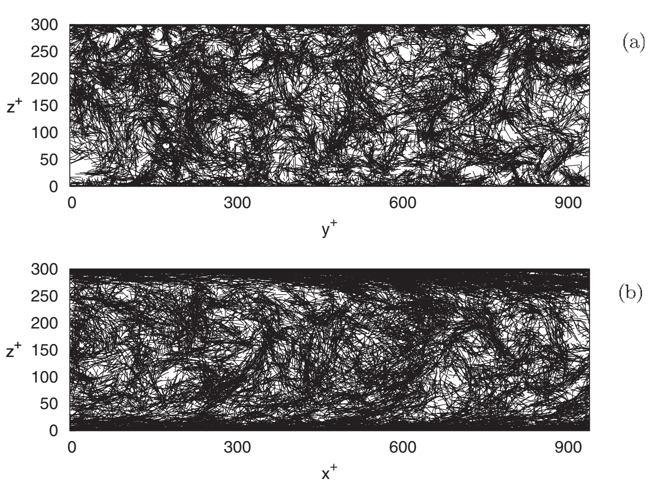

FIG. 1. Instantaneous fiber distribution at the end of the simulation ($\tau_p^+=5$, $\lambda=50$). Panels: (a) cross-sectional view (mean flow directed toward the reader; $0<x^+<200$) and (b) lateral view (mean flow directed from left to right; $600<y^+<750$).

Once in the near-wall region, fibers segregate into elongated streaks, as shown in Fig. 2. Visual inspection of this figure, and of Fig. 2(b) in particular, does not reveal preferential orientation along the streamwise direction for segregated fibers. In wall-bounded turbulence, it is a well-known fact that such streaks correlate spatially with regions of low-speed fluid velocity (low-speed streaks): this feature has been observed for both spherical and elongated particles. In the latter case, however, only qualitative visualizations[7–9] are available. An example of such visualizations is given in Fig. 3. Specifically, Fig. 3(a) shows fiber distribution around the cross-sectional plane $x^+\simeq 100$, superposed to the wall-normal fluid velocity. In this figure, only fibers located in the slab $\Delta x^+=100\pm 20$ are visualized, and grayscale contours (yellow-to-blue contours in the online color version) are used to mark regions of wall-normal fluid transfer produced by vortices. Figure 3(b) shows fiber distribution around the wall-parallel plane $z^+\simeq 6.4$ superposed to the streamwise fluid velocity fluctuations. In this figure, only fibers located in the slab $\Delta x^+=6.4\pm 3$ are visualized, and grayscale contours (yellow-to-blue contours in the online color version) are used to mark low/high-speed regions. Note that Figs. 1–3 are all taken at the same time.

To provide a quantitative analysis, in Fig. 4 we show the correlation between the normalized probability density function (PDF) of fiber position and the fluctuation of the streamwise velocity, $(u_x^+)'$, in the wall region ($5\leq z^+\leq 15$). For ease

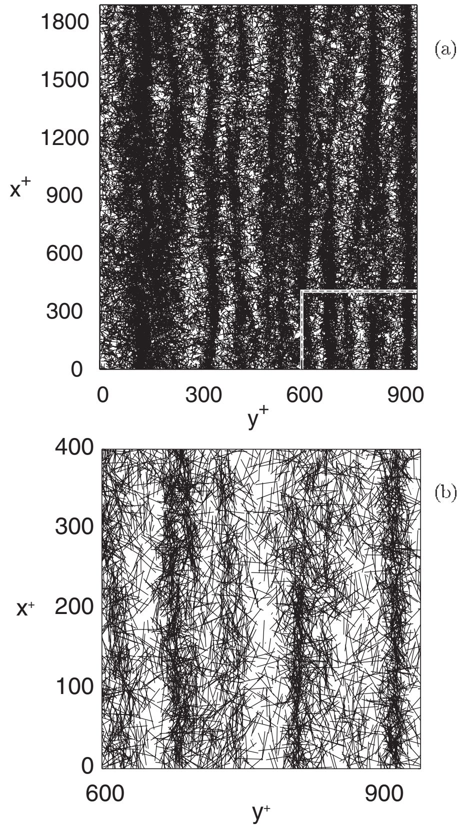

FIG. 2. Top view of instantaneous fiber distribution at the end of the simulation ($\tau_p^+=5$, $\lambda=50$, $0<z^+<25$, mean flow directed bottom up). For visualization purposes, panel (b) provides a close-up view of fiber distribution in the region highlighted in panel (a).

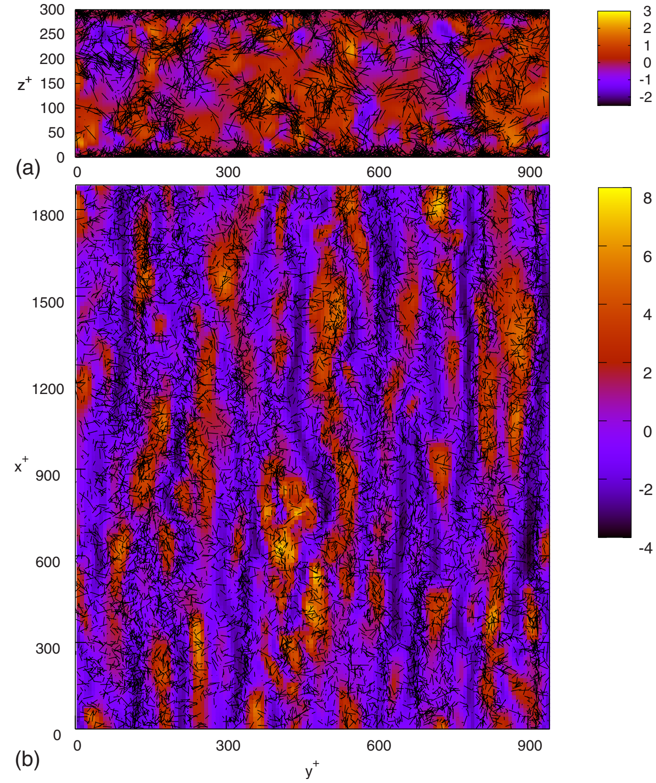

FIG. 3. (Color online) Instantaneous distribution of fluid velocity fluctuations and fibers. Panels: (a) contour plot of wall-normal fluid velocity fluctuations and fiber distribution in the cross-sectional y-z plane taken at $x^+\simeq 100$ and (b) contour plot of streamwise fluid velocity fluctuations and fiber distribution in the cross-sectional x-y plane taken at $z^+\simeq 6.4$ Regions of large positive/negative velocity fluctuations are represented in light/dark gray (yellow/blue in the online color version).

of visualization, only profiles for $\tau_p^+=1$ and $\tau_p^+=30$ are shown in the main panel. PDF profiles were computed as follows: (I) we subdivided the region $5\leq z^+\leq 15$ in 10 equally spaced slabs and calculated the average streamwise velocity of the fluid $\bar{u}_{\text{slab}}(z)$ in each slab, (II) we determined the slab containing the fiber center, (III) we computed the local streamwise velocity fluctuation of the fluid $u'(x,y,z)=u(x,y,z)-\bar{u}_{\text{slab}}(z)$ in the position of the fiber, (IV) we counted the number of fibers associated with each value of $u'(x,y,z)$ and normalized it by the total number of fibers located into each slab.

Figure 4 demonstrates that, regardless of the aspect ratio, all PDF profiles show a peak for the same negative value of fluctuating streamwise velocity. It also demonstrates that both shape and peak value attained by each PDF depend on fiber inertia, as highlighted by the inset panel. Being characterized by the narrowest PDF and maximum peak value, the $\tau_p^+=30$ fibers exhibit the strongest tendency to segregate into streaks; whereas the $\tau_p^+=1$ fibers, whose PDF is rather flat and has minimum peak value, are those that segregate the least. These observations indicate that, just like preferential distribution, fiber segregation into low-speed streaks is an inertia-dominated process and does not depend on elongation.

B. Local fiber segregation

The relative tendency of fibers to segregate in a turbulent flow field, shown in Figs. 1 and 2, can be quantified using the following parameter:[17]

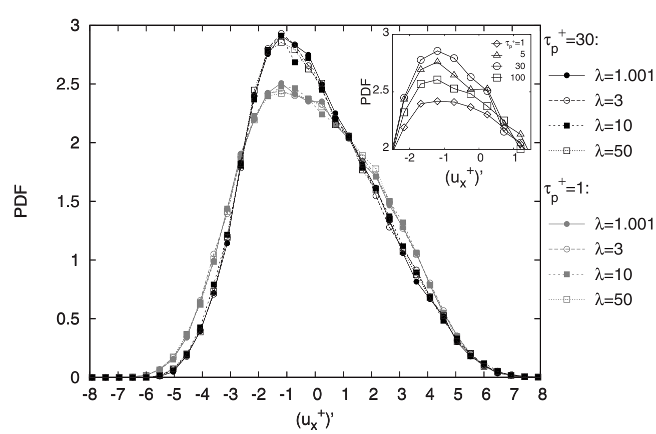

FIG. 4. Fiber number density distribution as a function of fluctuating streamwise velocity, $(u_x^+)'$, in the wall region ($5<z^+<15$). Black lines/symbols refer to the $\tau_p^+=30$ fibers; gray lines/symbols refer to the $\tau_p^+=1$ fibers (profiles for $\tau_p^+=5$ fibers and for the $\tau_p^+=100$ fibers are not shown to visualize better the behavior of the PDF in the peak region). The inset shows the behavior of the PDF in the peak region for fibers with different inertia (all values of τ_p^+ are shown) in the reference $\lambda=50$ case: peak value increases from $\tau_p^+=1$ up to $\tau_p^+=30$ with subsequent decrease for $\tau_p^+=100$.

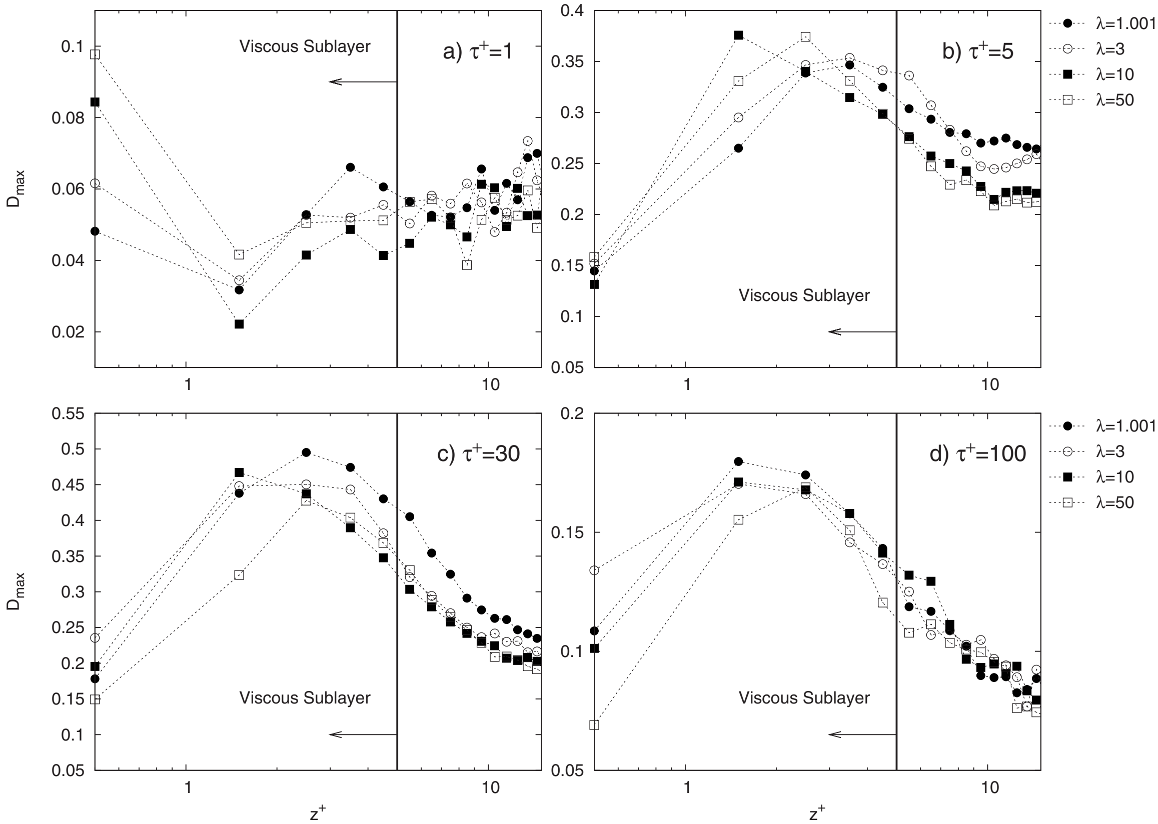

FIG. 5. Wall-normal maximum deviation from randomness. Panels: (a) $\tau_p^+=1$, (b) $\tau_p^+=5$, (c) $\tau_p^+=30$, and (d) $\tau_p^+=100$.

$$D = \frac{\sigma - \sigma_{\mathrm{Poisson}}}{\mu}, \tag{13}$$

where σ represents the standard deviation for the actual fiber number density distribution; $\sigma_{\mathrm{Poisson}}$ represents the standard deviation for a Poisson distribution, which corresponds to a purely random distribution of the same average number of fibers; and μ is the mean fiber number density. Clearly, the larger is the value of D and the stronger is segregation. In our simulations, we have tried to extend the use of D, originally devised for and applied to two-dimensional homogeneous isotropic flow regions,[17,18] to the near-wall region, where inhomogeneities arise in the direction perpendicular to the wall. The fiber number density distribution is thus computed on a three-dimensional grid containing N_{cell} cells of volume Ω_{cell} covering the entire computational domain. The grid is independent of the Eulerian grid used by the flow solvers, and the volume Ω_{cell} is varied by changing the streamwise and the spanwise lengths of the cell, whereas the wall-normal length is maintained to a uniform thickness: this avoids the introduction of an additional averaging scale in the wall-normal direction. As in the bidimensional case, the value calculated for D depends on the cell size. Because of this dependency, the segregation parameter cannot provide an absolute, clearcut quantification of fiber segregation; rather it should be used just to identify and compare differences in the tendency of fibers to segregate in a turbulent flow field according to their inertia and elongation. Taking this into account, the cell size dependency can be partially overcome by computing the fiber number density distribution for several values of Ω_{cell} and keeping only the largest value of D, referred to as $D_{\max}$ hereinafter.[18–20]

In Fig. 5, we show the behavior of $D_{\max}$ as a function of the wall-normal coordinate, z^+, for all cases considered in the (λ, τ_p^+)-space. Profiles are averaged both in space, over the homogeneous directions, and in time, over the last 200 time units of the simulations. As expected, segregation reaches a maximum inside the viscous sublayer ($z^+ < 5$), suggesting that such build-up is driven by inertia. Indeed, the larger values of $D_{\max}$ are obtained for the $\tau_p^+=30$ fibers, which exhibit the highest tendency to undergo low-speed streak segregation; whereas small values are obtained for the $\tau_p^+=1$ fibers, which exhibit the lowest tendency to undergo low-speed streak segregation (see Fig. 4). Once in the viscous sublayer, however, elongation becomes important in determining the location and the magnitude of maximum segregation. Changes in the aspect ratio produce nonmonotonic modifications and cross-overs between profiles indicating that, locally, the influence of wall turbulence on fibers is strongly affected by λ and τ_p^+. To quantify this influence, in Fig. 6 we show the mean value of $D_{\max}$ as a function of fiber elongation in the viscous sublayer. It is confirmed that, for a given fiber elongation, near-wall segregation experiences a monotonic increase up to $\tau_p^+=30$ followed by a decrease for $\tau_p^+=100$. Compared to the reference case of spherical particles, the influence of λ is maximum for the $\tau_p^+=30$ fibers, with an overall 17% variation in $D_{\max}$, and minimum for the $\tau_p^+=5$ fibers, with an overall 8% variation.

The results just discussed show the presence of a specific

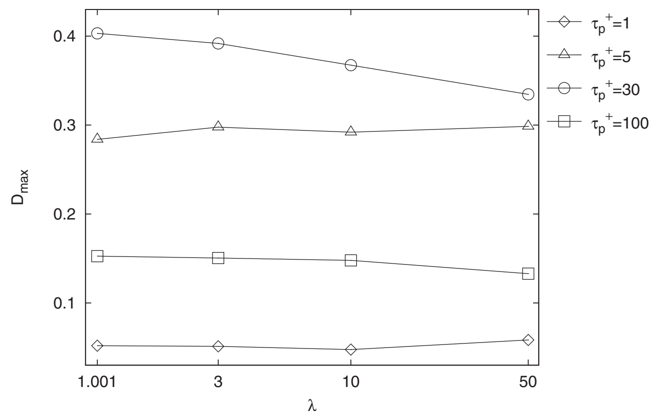

FIG. 6. Averaged maximum deviation from randomness in the near-wall region ($0<z^+<5$). Values in the (λ,τ_p^+)-space are averaged over the homogeneous directions, and in time, over the last 200 wall time units of the simulation. Symbols: (◇) $\tau_p^+=1$, (△) $\tau_p^+=5$, (○) $\tau_p^+=30$, and (□) $\tau_p^+=100$.

parameter range in which the effect of inertia combines with the effect of elongation; this gives rise to a nontrivial behavior eventually leading to significant quantitative changes in the near-wall dispersion process. Statistics shown so far may provide useful indications on the link between fiber accumulation into specific regions in the buffer layer and fiber deposition to a wall, which will be analyzed in the next section. Specifically, (I) they confirm that there is a strong correlation between coherent wall structures, local fiber segregation, and subsequent deposition phenomena; and (II) they demonstrate that fiber deposition is initially dominated by inertia-induced segregation and accumulation into specific flow regions close to the walls. Only afterwards fibers are driven to the walls.[19]

C. Fiber deposition rates and wall accumulation

As already observed by Mortensen *et al.*,[8] almost all translational velocity statistics are negligibly affected by changes in fiber elongation; the same being true for acceleration statistics (not shown here). One important exception, however, is given by the fiber wall-normal translational velocity, w'_p. Besides being strongly dependent on the fiber response time, this quantity is also significantly influenced by λ, as shown in Fig. 7 for fibers with $\tau_p^+=5$ and $\tau_p^+=30$ (again, similar curves are obtained for the other fiber categories, but they are not shown here for brevity). Note that the profiles in this figure were smoothed out by time-averaging over the last 200 wall time units of the simulation. Such time-averaging procedure was adopted for ease of comparison and for visualization purposes only: the profiles considered refer to a statistically developing condition for the fiber concentration and, thus, w'_p is a time-dependent quantity which asymptotically tends to zero as the steady-state condition is approached. In the $\tau_p^+=5$ case, the aspect ratio produces a nonmonotonic variation in w'_p leading to a maximum increase for

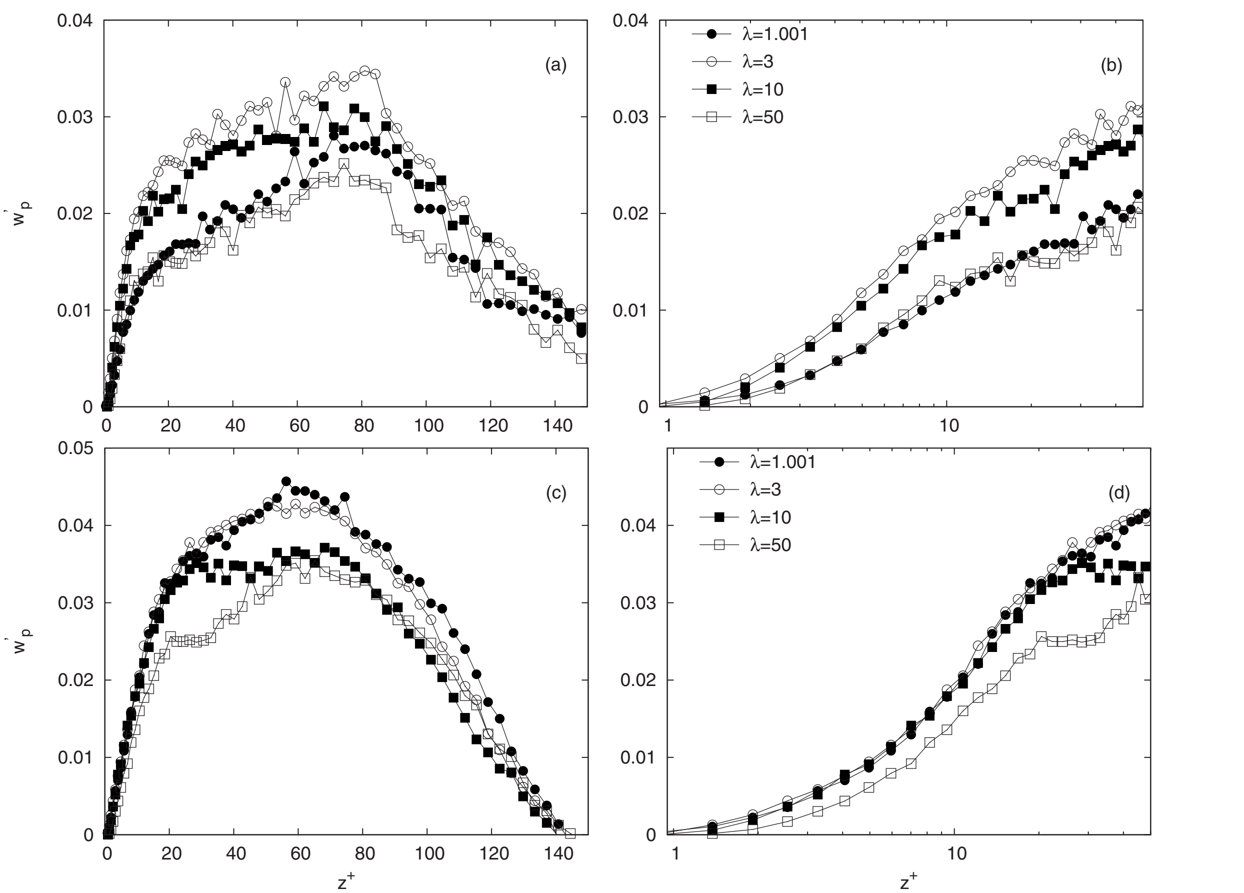

FIG. 7. Mean wall-normal translational velocity, w'_p, for the $\tau_p^+=5$ fibers [panels (a) and (b)], and for the $\tau_p^+=30$ fibers [panels (c) and (d)]. Panels (b) and (d) show a close-up view of the profiles in the near-wall region (log-lin plot).

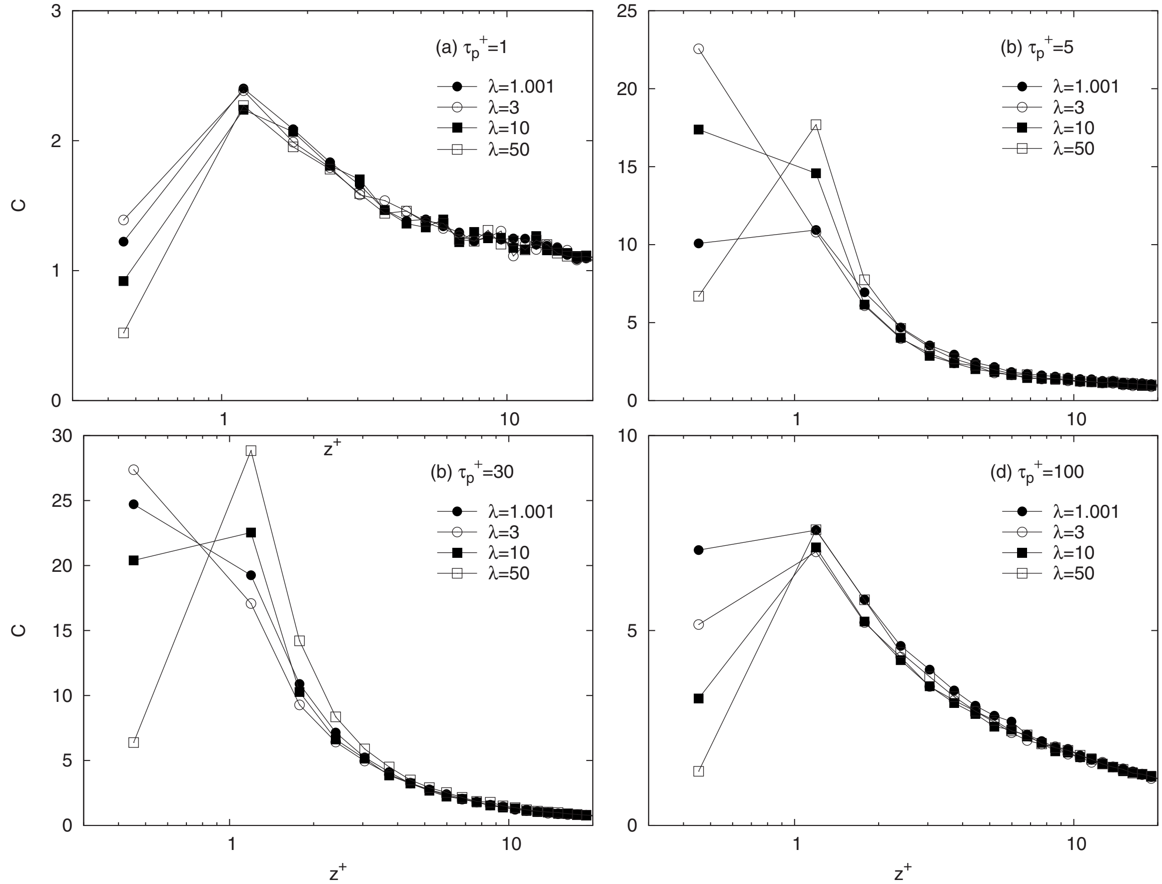

FIG. 8. Wall-normal fiber concentration profiles (taken at $t^+=1056$). Panels: (a) $\tau_p^+=1$, (b) $\tau_p^+=5$, (c) $\tau_p^+=30$, and (d) $\tau_p^+=100$.

$\lambda=3$ and a subsequent decrease for $\lambda=10$ and for $\lambda=50$: in this latter case, the velocity profile overlaps with that of spherical particles in the buffer layer. Conversely, for the larger $\tau_p^+=30$ fibers (and for the not-shown $\tau_p^+=100$ fibers) we observe a monotonic decrease as λ increases. In our opinion, these observations are interesting in the light of the discussion made for Figs. 1(a) and 3(a). Differences in w_p' suggest that, once centrifuged out of the vortex core because of inertia, fibers tend to occupy different areas in the periphery of the vortex according to their own elongation. This would mean that fibers with different aspect ratio attain different peripheral location and *see* a different local flow field, thus being exposed to different turbulent fluctuations.

The complex dependency of w_p' on both τ_p^+ and λ produces remarkable changes in the rate at which fibers travel toward the wall and, in turn, modify the build-up of fibers in the near-wall region: this is shown by the instantaneous concentration profiles (computed as volumetric fiber number density) of Fig. 8. From a quantitative viewpoint, the most evident changes occur in the very near-wall region, within a few wall units from the wall: each profile develops a peak of concentration which is located at different positions depending on the aspect ratio, and the peak value changes according to the variations in w_p' discussed above. Outside the viscous sublayer, variations are less evident and, again, the elongation of the fiber does not seem to play an important role.

According to the chain of physical mechanisms by which fibers are transferred to the wall, the degree of fiber segregation also influences the rate at which fibers deposit (i.e., their deposition flux). It is thus consequential to combine the quantitative description of fiber segregation to the quantitative prediction of fiber deposition rate. The deposition rate of noninteracting fibers is proportional to the ratio between the fiber mass transfer rate on the wall, J, and the mean bulk concentration of fibers, C. The constant of proportionality, named deposition coefficient $k_d=-J/C$, represents a deposition velocity.[21] Figure 9 shows the nondimen-

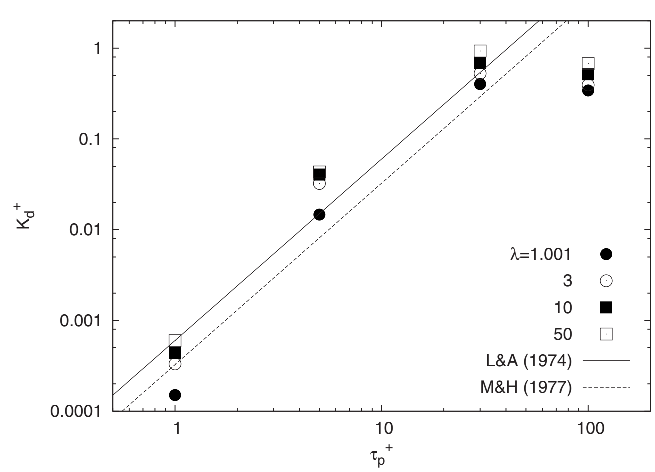

FIG. 9. Deposition coefficient, k_d^+, as a function of fiber elongation (given by λ) and fiber inertia (given by τ_p^+).

sional values of the deposition coefficient, k_d^+, in the (λ, τ_p^+)-space. For comparison purposes, two empirical correlations proposed by Liu and Agarwal[22] [$k_d^+=6\times10^{-4}(\tau_p^+)^2$, solid line] and by McCoy and Hanratty[23] [$k_d^+=3.25\times10^{-4}(\tau_p^+)^2$, dashed line] are also included in the figure. These correlations were derived from a large collection of experimental deposition data from fully developed turbulent pipe flow,[21] and are valid for spherical particles in the diffusion-impaction deposition regime. In this regime, which is characterized by Stokes numbers varying from about 0.3 to about 30, the deposition rate scales with the square of the nondimensional response time.

The trend highlighted by Fig. 9 is similar to that seen in Figs. 2, 5, and 6, which refer to the same simulation time span: again, the $\tau_p^+=30$ fibers exhibit the highest deposition rate. This happens because these fibers are the most responsive to near-wall turbulence in terms of segregation and preferential distribution. Fibers with smaller or larger inertia (but same elongation) are not able to respond in this optimal way, either because they behave more like tracers with strong stability against nonhomogeneous distribution and near-wall concentration (the $\tau_p^+=1$ fibers, in particular), or because they are too big to interact with the fine turbulence structures in the buffer layer (the $\tau_p^+=100$ fibers, for instance). There is also a clear effect of elongation: higher values of the aspect ratio correspond to higher values of the deposition coefficient, in agreement with the findings of Zhang *et al.*[7] This effect seems to fade as the response time of the fibers increases: we remind that, for a given τ_p^+, the mass of a fiber increases with its elongation so longer fibers have higher inertia. In general terms, the results shown in this section indicate that the degree of fiber responsiveness to segregation and preferential distribution induced by the flow structures is strongly (and directly) correlated with the rate at which fibers deposit.

D. Fiber orientation and alignment frequency

To investigate further the role of λ and τ_p^+, we analyzed fiber orientation statistics. For the sake of completeness, we show first the absolute value of the mean direction cosines for $\tau_p^+=5$ and $\tau_p^+=30$ (see Fig. 10). Profiles agree with those already shown by Mortensen *et al.*[8] for fibers with the same dimensionless response time and aspect ratio dispersed in a slightly higher Reynolds number flow. Note that the profiles relative to fibers with $\lambda=50$ are presented for the first time. It is confirmed that fibers tend to align in the streamwise directions and that this preferential orientation increases with aspect ratio and decreases with inertia, as shown by Figs. 10(a) and 10(b). This tendency affects fiber spanwise orientation. As shown by Figs. 10(c) and 10(d), higher-inertia fibers are less oriented in the spanwise direction: following Mortensen *et al.*,[8] spanwise fluctuations are relatively weak and their capability of altering the alignment of a fiber is reduced as fiber inertia increases. Also higher-inertia fibers are more oriented toward the wall, as demonstrated by Figs. 10(e) and 10(f). In an effort to go beyond these observations, we focus on the orientation frequency, defined as the overall time spent by the fibers in a given position of alignment with respect to the mean flow. To perform this calculation, we proceeded for each fiber category in the following way: (I) the alignment of each fiber was classified by subdividing the absolute value of the direction cosines, $|\cos(\theta_i)|$, which determine the orientation of the particle with respect to the Cartesian axes (see Fig. 11), into 10 equally spaced bins, e.g., first bin in the range [0,0.1], second bin in the range [0.1,0.2], etc. Fibers are tagged as aligned with a given direction, x_i, if they fall in the bin where $|\cos(\theta_i)|$ is in the range [0.9,1] (*alignment* bin). (II) The orientation of each fiber and the corresponding bin are obtained at every time step over a long period of time ($T^+=200$ at the end of the simulation); a time-counter is then updated to compute the overall time, $t^+(i,j,k)$, spent by the ith fiber of the jth category in the kth bin. (III) The mean time per bin is computed as $t^+(j,k)=\sum_{i=1}^{N(k)} t^+(i,j,k)$, where $N(k)$ is the number of fibers counted in the kth bin; then its percentage value is obtained as $\%t^+=t^+(j,k)/T^+$. Such procedure was applied focusing on two specific regions of the flow: a near-wall region ($z^+<10$ from the wall) and a core region across the channel centerline ($100<z^+<200$). In Figs. 12–14, we show the results obtained in the near-wall region (where the most interesting observations can be made) for $|\cos(\theta_x)|$, $|\cos(\theta_y)|$, and $|\cos(\theta_z)|$, respectively. All cases in the (λ, τ_p^+)-space are shown. For completeness, an inset has been added in each panel to show results obtained in the channel centerline. In this region, there is almost no mean shear and turbulence is nearly homogeneous and isotropic, so preferential fiber orientation is never observed. Only for $\tau_p^+=1$ and $\tau_p^+=5$ fibers, whose specific density is $\mathcal{O}(10^1 \div 10^2)$, a slight increase in $\%t^+$ when $|\cos(\theta_x)|\in[0.9,1]$, $|\cos(\theta_y)|\in[0,0.1]$, and $|\cos(\theta_z)|\in[0,0.1]$ occurs, as shown by insets of Fig. 12(a)–12(c), respectively.

Let us focus on the streamwise orientation frequencies (Fig. 12). Interesting observations can be made. First: even though the most probable fiber orientation is in the streamwise direction, as demonstrated by Zhang *et al.*[7] and by Mortensen *et al.*,[8,9] fibers are aligned with the mean flow at most 50% of the time in the most favorable case [$\tau_p^+=5$, $\lambda=50$, Fig. 12(b)]; orientation frequencies otherwise decrease, either because the aspect ratio decreases (for instance, $\%t^+$ falls to about 30% for the $\tau_p^+=5$ fibers with $\lambda=3$) or because the inertia decreases (for instance, $\%t^+$ falls to about 30% also for the $\tau_p^+=30$ fibers with $\lambda=50$). These percentages indicate that the position of near-wall alignment imposed by the streamwise fluctuations of the flow, though statistically probable, is quite "unstable" and cannot be maintained for very long times.

Second observation: elongation influences orientation frequencies only for the two lower inertia fibers [Figs. 12(a) and 12(b)], whereas negligible modifications are observed for the two higher-inertia fiber categories [Figs. 12(c) and 12(d)]; therefore, longer fibers have larger probability of being oriented in the streamwise direction provided that their inertia is below a threshold value (between $\tau_p^+=5$ and $\tau_p^+=30$). If this condition is not met, the fiber may disengage from turbulence dynamics more easily making near-wall alignment difficult. Note that, since the direction cosines are nonlinear functions, equally spaced bins for $|\cos(\theta_x)|$ corre-

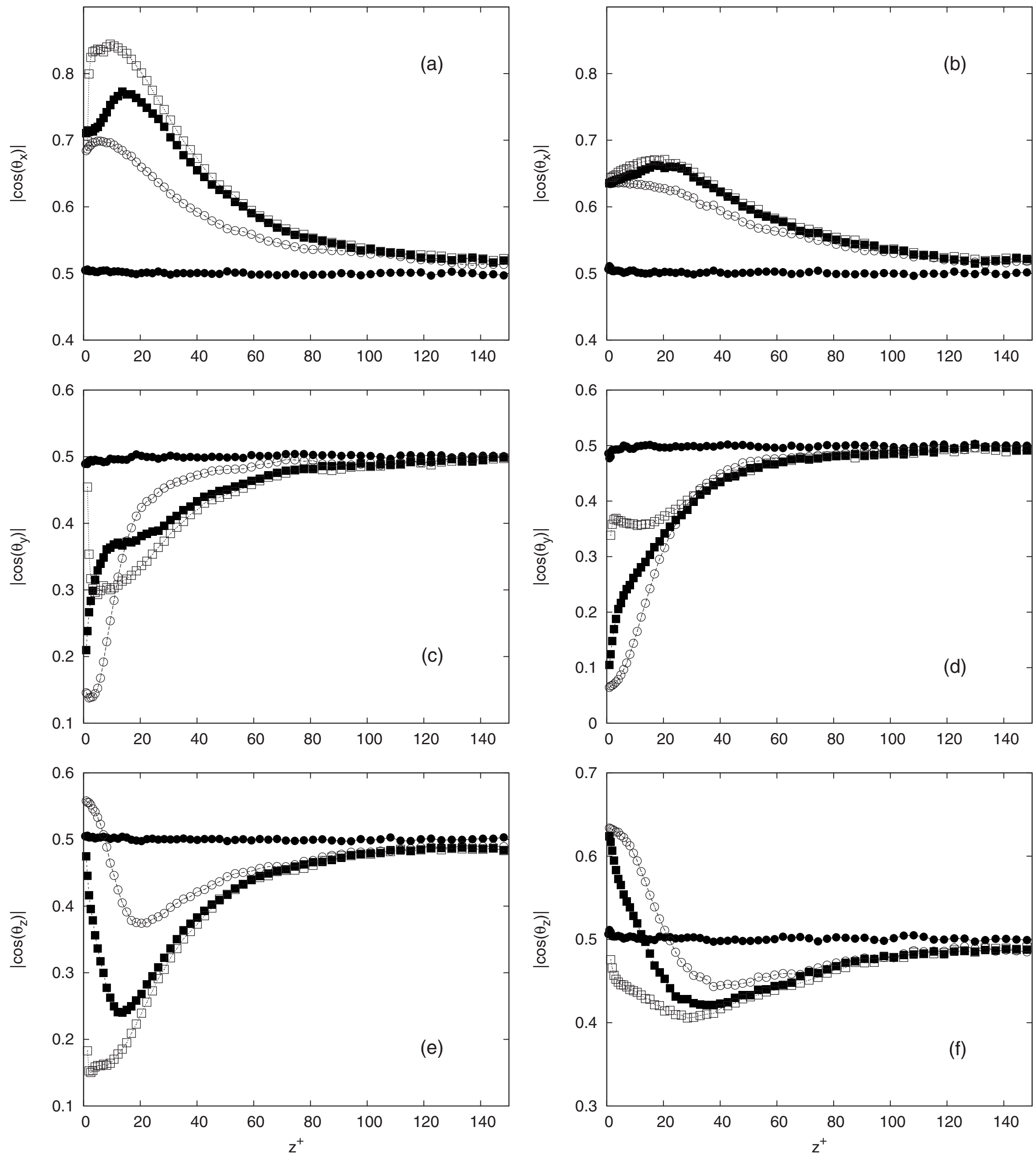

FIG. 10. Absolute values of mean direction cosines. Panels: [(a) and (b)] $|\cos(\theta_x)|$; [(c) and (d)] $|\cos(\theta_y)|$; and [(e) and (f)] $|\cos(\theta_z)|$. Symbols: (●) $\lambda=1.001$, (○) $\lambda=3$, (■) $\lambda=10$, and (□) $\lambda=50$.

spond to bins of different amplitude for θ_x, the alignment bin being wider than the others. We thus expect that results computed considering equally spaced bins for θ_i would lead to the same (probably even more striking) qualitative conclusion.

It is interesting to correlate the results just discussed with those obtained for the orientation frequencies in the spanwise and wall-normal directions. Mortensen *et al.*[8,9] have shown that the most probable kind of near-wall motion for an ellipsoidal particle is rotation about the spanwise axis (in the x-z plane) driven by the coupled effect of mean shear and streamwise turbulent fluctuations. The same authors have also shown that this motion may become less pronounced according to fiber inertia: *slower* particles, i.e., par-

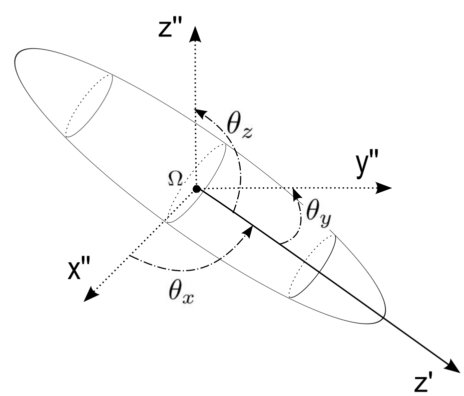

FIG. 11. Schematics of angles θ_i used to compute the direction cosines. The z' axis is used to determine fiber orientation with respect to a comoving frame (x'', y'', z'') with origin in the fiber's center of mass, Ω, and always parallel to the inertial (Eulerian) frame of reference.

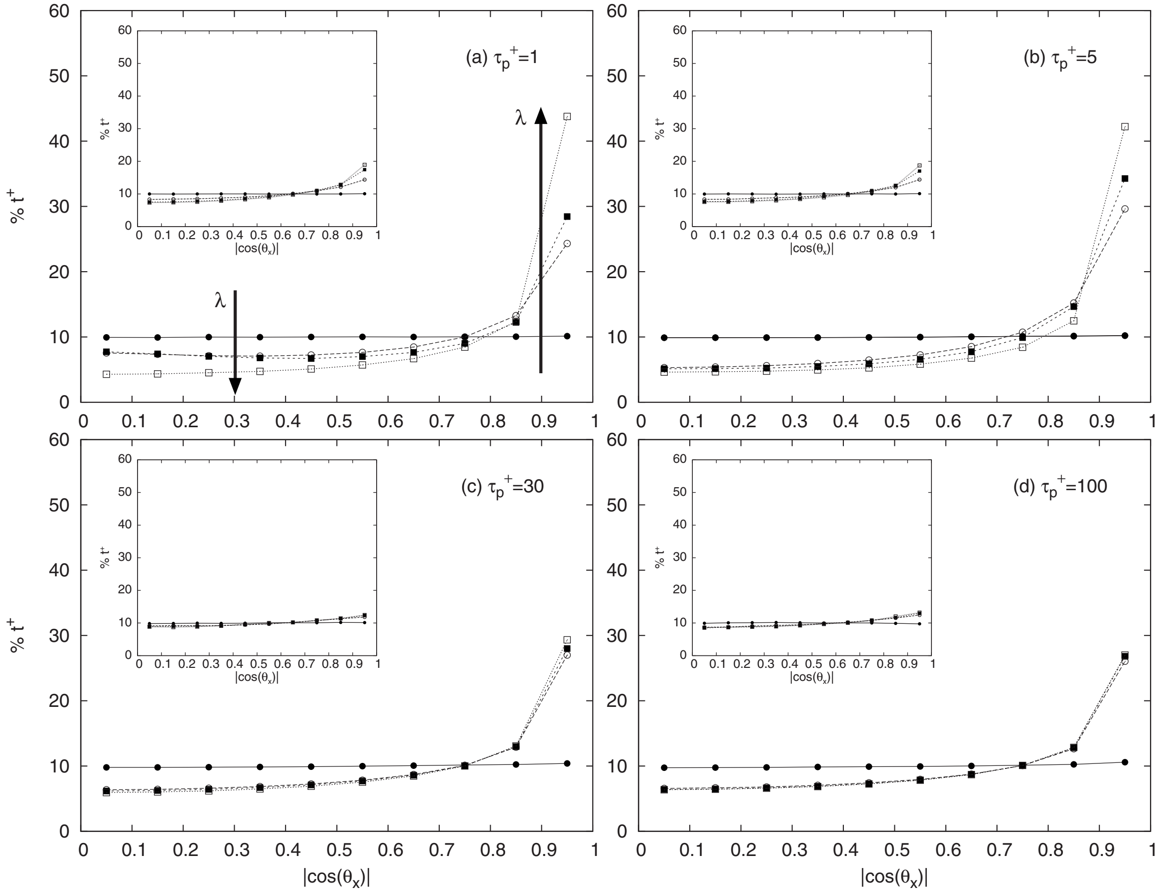

FIG. 12. Streamwise orientation frequency (percent values) in the near-wall region ($z^+ < 10$). For comparison purposes, percent values in the center of the channel are also shown in the inset of each panel. Panels: (a) $\tau_p^+=1$; (b) $\tau_p^+=5$; (c) $\tau_p^+=30$; and (d) $\tau_p^+=100$. Symbols: (●) λ=1.001, (○) λ=3, (■) λ=10, and (□) λ=50.

ticles with higher inertia (corresponding to $\tau_p^+=30$ in Mortensen *et al.*;[8] and to $\tau_p^+=10$ in Mortensen *et al.*[9])—are less oriented in the spanwise direction and less aligned with the wall as compared to *faster* particles, i.e., particles with lower inertia (corresponding to $\tau_p^+=5$ in Mortensen *et al.*;[8] and to $\tau_p^+=0.5$ in Mortensen *et al.*[9]). Figure 13 supports these conclusions in that (I) the orientation frequency is highest in correspondence of the *nonalignment* bin [$|\cos(\theta_y)|$ in the range [0:0.1]]; and (II) the nonalignment bin is sampled more often by the slower fibers ($\tau_p^+=30$ and $\tau_p^+=100$). However, the figure also shows that fibers can maintain their position in the vertical *x*-*z* plane for rather short times, this being true for all fiber categories but those characterized by aspect ratio λ=3: lateral tilting of these fibers is nearly suppressed so they actually spend most of time (up to 70% for fibers with $\tau_p^+=30$ or $\tau_p^+=100$) lying in the vertical plane. As a final remark on Fig. 13, we note that, for a given value of the aspect ratio, preferential sampling of the nonalignment bin is a nonmonotonous function of fiber inertia: this can be easily seen by comparing the values of $\%t^+$ for $\tau_p^+=100$ with those for $\tau_p^+=5$ and $\tau_p^+=30$.

To conclude our analysis on orientation, we consider wall-normal orientation frequencies (Fig. 14). It is apparent that frequencies in the near-wall region change significantly as fiber inertia increases. Let us consider the $\tau_p^+=1$ case first—Fig. 14(a). Values of $\%t^+$ increase with increasing fiber elongation when the direction cosine $|\cos(\theta_z)|$ is in the range [0:0.1]: this means that longer fibers are found more frequently aligned with the wall suggesting a preferred seesaw-like rotation, characterized by alternate oscillations of the fiber tips, as they are advected downstream. The trend is enhanced for the case of $\tau_p^+=5$ fibers with λ=50, but damped for smaller aspect ratios [Fig. 14(b)]. This may be due to the fact that the residual wall-normal turbulent fluctuations in the proximity of the wall are not strong enough to lift the longer fibers and induce planar rotation about the spanwise axis. Orientation frequencies of slower fibers [$\tau_p^+=30$ but also $\tau_p^+=100$, shown in Fig. 14(c) and Fig. 14(d), respectively] distribute almost evenly over all bins, with a slight increase in correspondence of the alignment bin: this indicates that fibers with sufficient inertia, i.e., large specific density, change continuously their orientation with respect to the wall suggesting a preferred tumbling-type clockwise rotation as they are advected downstream. Note that fiber elongation is always important in determining spanwise and wall-normal orientation frequencies. This may be due to the fact that the turbulent fluctuations in these directions are not strong enough to stabilize fibers and damp elongational effects. As discussed previously, stabilization without elongational effects can be achieved in the streamwise direction, where turbulent fluctuations are stronger; yet it would require sufficient inertia.

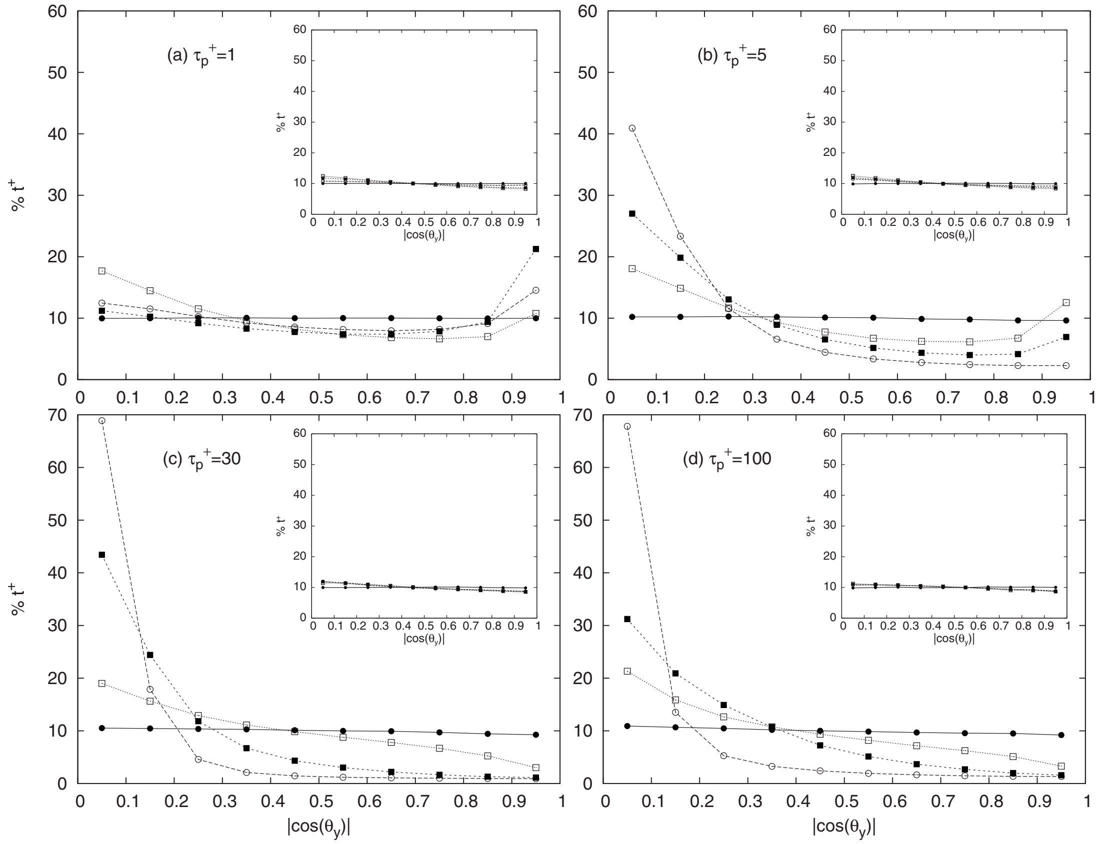

FIG. 13. Spanwise orientation frequency (percent values) in the near-wall region ($z^+<10$). For comparison purposes, percent values in the center of the channel are also shown in the inset of each panel. Panels: (a) $\tau_p^+=1$; (b) $\tau_p^+=5$; (c) $\tau_p^+=30$; and (d) $\tau_p^+=100$. Symbols: (●) $\lambda=1.001$, (○) $\lambda=3$, (■) $\lambda=10$, and (□) $\lambda=50$.

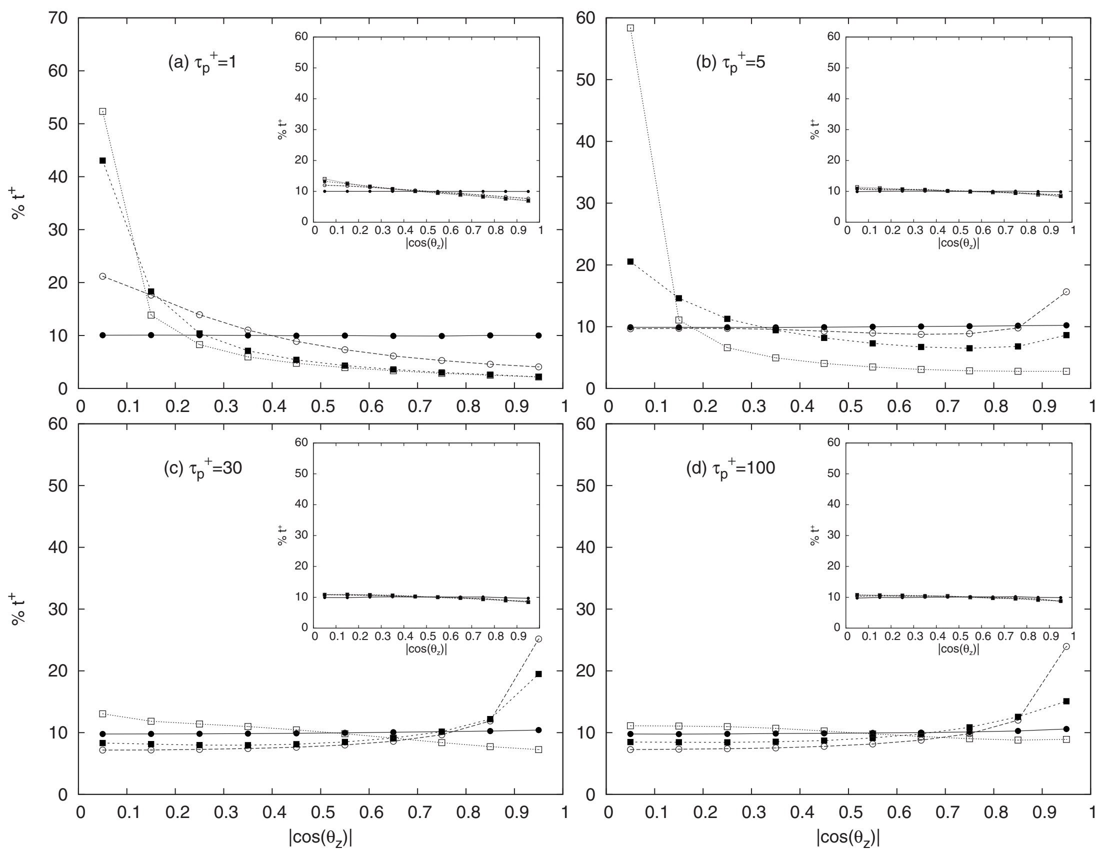

FIG. 14. Wall-normal orientation frequency (percent values) in the near-wall region ($z^+<10$). For comparison purposes, percent values in the center of the channel are also shown in the inset of each panel. Panels: (a) $\tau_p^+=1$; (b) $\tau_p^+=5$; (c) $\tau_p^+=30$; and (d) $\tau_p^+=100$. Symbols: (●) $\lambda=1.001$, (○) $\lambda=3$, (■) $\lambda=10$, and (□) $\lambda=50$.

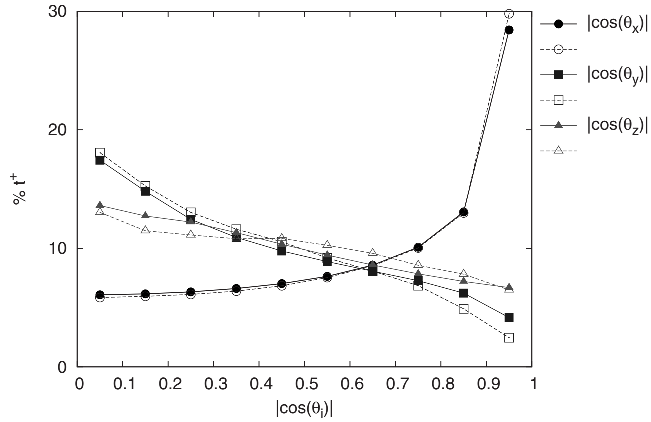

FIG. 15. Orientation frequencies (percent values) in the near-wall region ($z^+<10$) for $\tau_p^+=30$ fibers with $\lambda=50$. Open symbols refer to orientation frequencies computed only for fibers segregated into low-speed streaks. Symbols: (●,○) $|\cos(\theta_x)|$, (■, □) $|\cos(\theta_y)|$, and (▲, △) $|\cos(\theta_z)|$.

Results similar to those shown in Figs. 12–14 are obtained when orientation frequencies are computed only for fibers segregated into low-speed streaks, i.e., for fibers sampling near-wall regions of lower-than-mean streamwise fluid velocities. As an example, in Fig. 15 the near-wall conditional orientation frequencies of the $\tau_p^+=30$ fibers with $\lambda=50$ (open symbols) are compared against their unconditional counterparts (computed considering all fibers within the same region of the flow, namely, $z^+<10$). Profiles almost overlap, meaning that segregation into fluid streaks does not produce a significant stabilizing effect on fiber rotational motion.

In our opinion, such observables are important to interpret, from a physical viewpoint, the combined effect of fiber shape and inertia on macroscopic phenomena such as fiber wall accumulation and fiber segregation, which depend on the nature of fiber dynamics in connection with turbulence dynamics.[10]

IV. CONCLUSIONS AND FUTURE DEVELOPMENTS

In the present work, the dynamics of prolate ellipsoidal particles dispersed in a turbulent channel flow was analyzed using DNS and Lagrangian fiber tracking. Prolate ellipsoids were chosen because they reproduce quite reasonably the behavior of rigid elongated fibers in a number of applications of both scientific and engineering interest. Results obtained for several combination of values sampling the (λ, τ_p^+)-space indicate clearly that the coupling between the translation motion and the rotational motion of elongated fibers changes significantly their wallward flux by changing the mean fiber wall-normal velocity. This effect, which can ultimately be ascribed to the shape of the fibers, adds to that due to their inertia and, compared to the case of spherical particles, modifies from a quantitative viewpoint the build-up of fibers at the wall and the deposition rates. Such observables can be explained by looking at fiber rotational dynamics: as shown by the analysis of the near-wall fiber orientation frequencies, the preferred condition of streamwise alignment with the mean flow is unstable and can be maintained for rather short times before fibers are forced to rotate around the spanwise axis by the shear-induced wall-normal velocity gradient, thus changing their local spatial distribution. The main future development of this work is the inclusion of two-way coupling effects in the simulations. Hopefully, through these new simulations it will be possible to provide a physical explanation to the mechanism of fiber-induced turbulent drag reduction, which has been observed in many experiments (see Ref. 2 for instance).

ACKNOWLEDGMENTS

Financial support from CIPE (Comitato Interministeriale per la Programmazione Economica) under Grant *Caratterizzazione ed abbattimento di inquinanti e analisi del rischio nei processi di lavorazione del legno*, and from the Regional Authority of Friuli Venezia Giulia under Grant *Nuove metodologie per la riduzione e la gestione di emissioni di COV e particolato per l'industria di pannelli di particelle e fibra di legno* are gratefully acknowledged.

[1] M. Parsheh, M. Brown, and C. K. Aidun, "On the orientation of stiff fibres suspended in turbulent flow in a planar contraction," J. Fluid Mech. **545**, 245 (2005).
[2] J. S. Paschkewitz, C. D. Dmitropoulos, Y. X. Hou, V. S. R. Somandepalli, M. G. Mungal, E. S. G. Shaqfeh, and P. Moin, "An experimental and numerical investigation of drag reduction in a turbulent boundary layer using a rigid rodlike polymer," Phys. Fluids **17**, 085101 (2005).
[3] P. J. Krochak, J. A. Olson, and D. M. Martinez, "Fiber suspension flow in a tapered channel: The effect of flow/fiber coupling," Int. J. Multiphase Flow **35**, 676 (2009).
[4] J. J. J. Gillissen, B. J. Boersma, P. H. Mortensen, and H. I. Andersson, "The stress generated by non-Brownian fibers in turbulent channel flow simulations," Phys. Fluids **19**, 115107 (2007).
[5] J. S. Paschkewitz, Y. Dubief, and E. S. G. Shaqfeh, "The dynamic mechanism for turbulent drag reduction using rigid fibers based on Lagrangian conditional statistics," Phys. Fluids **17**, 063102 (2005).
[6] J. S. Paschkewitz, Y. Dubief, C. D. Dmitropoulos, E. S. G. Shaqfeh, and P. Moin, "Numerical simulation of turbulent drag reduction using rigid fibers," J. Fluid Mech. **518**, 281 (2004).
[7] H. Zhang, G. Ahmadi, F. G. Fan, and J. B. McLaughlin, "Ellipsoidal particles transport and deposition in turbulent channel flows," Int. J. Multiphase Flow **27**, 971 (2001).
[8] P. H. Mortensen, H. I. Andersson, J. J. J. Gillissen, and B. J. Boersma, "Dynamics of prolate ellipsoidal particles in a turbulent channel flow," Phys. Fluids **20**, 093302 (2008).
[9] P. H. Mortensen, H. I. Andersson, J. J. J. Gillissen, and B. J. Boersma, "On the orientation of ellipsoidal particles in a turbulent shear flow," Int. J. Multiphase Flow **34**, 678 (2008).
[10] C. Marchioli and A. Soldati, "Mechanism for particle transfer and segregation in turbulent boundary layer," J. Fluid Mech. **468**, 283 (2002).
[11] A. Soldati and S. Banerjee, "Turbulence modification by large-scale organized electro-hydrodynamic flows," Phys. Fluids **10**, 1742 (1998).
[12] I. Gallily and A. Cohen, "On the orderly nature of the motion of nonspherical aerosol particles," J. Colloid Interface Sci. **68**, 338 (1979).
[13] H. Brenner, "The Stokes resistance of an arbitrary particle," Chem. Eng. Sci. **18**, 1 (1963).
[14] G. B. Jeffery, "The motion of ellipsoidal particles immersed in a viscous fluid," Proc. R. Soc. London, Ser. A **102**, 161 (1922).
[15] F. G. Fan and G. Ahmadi, "A sublayer model for wall deposition of ellipsoidal particles in turbulent streams," J. Aerosol Sci. **25**, 831 (1995).
[16] M. Shapiro and M. Goldenberg, "Deposition of glass fiber particles from turbulent air flow in a pipe," J. Aerosol Sci. **24**, 65 (1993).
[17] J. R. Fessler, J. D. Kulick, and J. K. Eaton, "Preferential concentration of heavy particles in a turbulent channel flow," Phys. Fluids **6**, 3742 (1994).
[18] P. Février, O. Simonin, and K. D. Squires, "Partitioning of particle velocities in gas-solid turbulent flows into a continuous field and a spatially uncorrelated random distribution: Theoretical formalism and numerical study," J. Fluid Mech. **533**, 1 (2005).

[19] A. Soldati and C. Marchioli, "Physics and modelling of turbulent particle deposition and entrainment: Review of a systematic study," Int. J. Multiphase Flow **35**, 827 (2009).
[20] M. Picciotto, C. Marchioli, and A. Soldati, "Characterization of near-wall accumulation regions for inertial particles in turbulent boundary layers," Phys. Fluids **17**, 098101 (2005).
[21] J. Young and A. Leeming, "A theory of particle deposition in turbulent pipe flow," J. Fluid Mech. **340**, 129 (1997).
[22] B. Y. Liu and J. K. Agarwal, "Experimental observation of aerosol deposition in turbulent flow," J. Aerosol Sci. **5**, 145 (1974).
[23] D. D. McCoy and T. J. Hanratty, "Rate of deposition of droplets in annular two-phase flow," Int. J. Multiphase Flow **3**, 319 (1977).